

OPEN

Abyssal oceanic circulation and acidification during the Middle Eocene Climatic Optimum (MECO)

Flaminia Cornaggia^{1*}, Simone Bernardini², Martino Giorgioni³, Gabriel L. X. Silva^{1,5},
André Istvan M. Nagy⁴ & Luigi Jovane¹

The Middle Eocene Climatic Optimum (MECO) is a global warming event that occurred at around 40 Ma and lasted about 500 kyr. We study this event in an abyssal setting of the Tasman Sea, using the IODP Core U1511B-16R, collected during the expedition 371. We analyse magnetic, mineralogical, and chemical parameters to investigate the evolution of the sea bottom conditions at this site during the middle Eocene. We observe significant changes indicating the response to the MECO perturbation. Mn oxides, in which Mn occurs under an oxidation state around +4, indicate a high *Eh* water environment. A prominent Mn anomaly, occurring just above the MECO interval, indicates a shift toward higher *pH* conditions shortly after the end of this event. Our results suggest more acid bottom water over the Tasman abyssal plain during the MECO, and an abrupt end of these conditions. This work provides the first evidence of MECO at abyssal depths and shows that acidification affected the entire oceanic water column during this event.

The Eocene (~56–34 Ma) was characterized by a gradual climatic cooling, accompanied by decreasing atmospheric *pCO*₂ and culminating with the onset of the Antarctic glaciation in the early Oligocene (33 Ma)^{1–5}. This trend was interrupted during the middle Eocene by a warm period known as Middle Eocene Climatic Optimum (MECO), with duration of ~500 kyr and a warmth peak at ~40 Ma^{6,7}. The MECO has been identified in several sedimentary records around the globe, including the South Pacific Ocean^{8,9}. It is related to an increase in seawater temperature, from the surface to deep bathyal depths, and increasing *pCO*₂ in the atmosphere^{10,11}. Moreover, significant changes in atmospheric and oceanic circulation dynamics and in the patterns of continental rainfall are recorded^{12,13}. However, classic climatic models fail to explain how such conditions could persist for several hundreds of thousand years¹⁴.

Southern Ocean (SO) circulation is extremely important for understanding the climatic evolution during the Eocene, and particularly during the MECO. The separation of Australia from Antarctica during the middle-late Eocene profoundly affected the circulation and made this region particularly sensitive to paleoceanographic changes^{4,15}. In this complex geological framework, the study of iron and manganese oxides in the sediments can provide important information, as they are strongly controlled by redox conditions and circulation¹⁶. Manganese oxides typically occur as cryptocrystalline materials, in which Mn precipitates under different oxidation states: Mn⁴⁺, Mn³⁺ and Mn²⁺¹⁷. Moreover, Mn is more sensitive than Fe to pH, and requires more basic conditions to precipitate. Therefore, an environment may promote the oxidation and precipitation of iron and not of manganese, if the pH is not sufficiently high^{18–21}. Accordingly, relatively small shift in the redox conditions can change significantly the equilibrium solubility of these elements and thus their presence or absence in the geological record. Microorganisms (i.e. bacteria and fungi) may also contribute to catalyse Mn and Fe oxidation²².

In this work we study bulk, clay, and oxide minerals within the MECO interval in a core from the IODP Core U1511B-16R, which offers a unique opportunity to study how the SO system responded to the MECO at abyssal depths. The IODP Hole U1511B was drilled during the Expedition 371 on the Tasman abyssal plain (TAP), located ~945 km east of Australia, at 4858 m depth (figure S1). Here we consider the middle Eocene interval encompassed between the sections 16R-4 and 16R-5, containing the base of the magnetochron C18n, which is the magnetostratigraphic marker of the MECO^{6,7,11,23–25}. This interval is characterized by a more clayey lithology,

¹Instituto Oceanográfico, Universidade de São Paulo, São Paulo, Brazil. ²Dipartimento di Scienze, Università Roma Tre, Rome, Italy. ³Instituto de Geociências, Universidade de Brasília, Brasília, Brazil. ⁴Departamento de AI, Faculdade Sul Americana, Goiânia, Brazil. ⁵Present address: INPE (Instituto Nacional de Pesquisas Espaciais), São José dos Campos (SP), Brazil. *email: flaminia.cornaggia@gmail.com

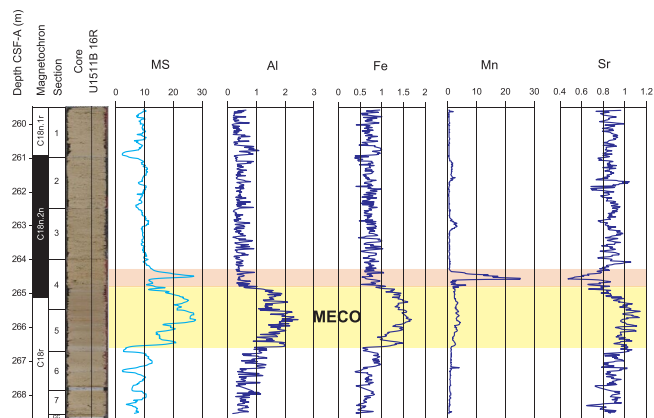


Figure 1. Litho- and magnetostratigraphy, and Magnetic Susceptibility (MS) of core U1511B-16R (from ref. ²⁶); and main elements abundance analysed by XRF from ref. ⁴⁶. The MECO interval is highlighted in yellow and the Mn anomaly just above it is highlighted in red.

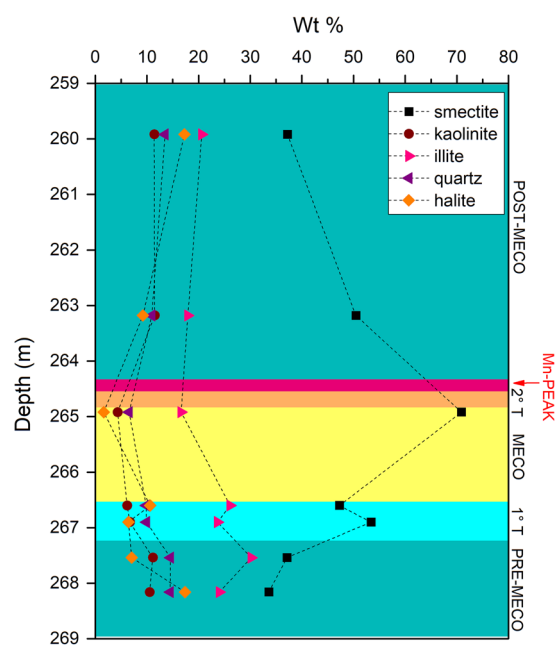


Figure 2. Conventional XRD results from the IODP Core U1511B_16R.

and increasing magnetic susceptibility (MS) and Natural Gamma Radiation (NGR)²⁶. We present a multimethodological and multidisciplinary investigation aimed at providing new data about the environmental changes affecting this system during the MECO. Our results show that a major change in deep-water circulation occurred over the TAP.

Results

Chemical and mineralogical compositions. At the optical microscope all samples appear as light yellowish-brown grained mixture of different minerals, with micrometric black and red grains. In the interval between 264.9–266.7 mbsf, the red grains are more abundant, making the colour of the sediment reddish-brown.

XRF-scanner data show a change in chemical composition in the 266.5–266.8 mbsf interval, which corresponds to the stratigraphic position of the MECO (Fig. 1 and S3). All the detrital elements (Al, Ti, Fe, K, and Si) increase, whereas Cl decreases, and Ca and Sr display various fluctuations. Of particular interest is Mn, which shows a slight increase within this interval and a prominent peak just above it encompassing several cm. The detrital elements increase and the overlying peak of Mn are also concomitant with high values of MS (Fig. 1).

Bulk XRPD results show abundant quartz, halite, and clay minerals in all the studied samples. Analyses performed on clay-separated fraction revealed illite, kaolinite and smectite (see supplements). A distinct increase in smectite respect to the other minerals occurs between 264.85–266.57 mbsf, corresponding to the stratigraphic position of the MECO (Fig. 2).

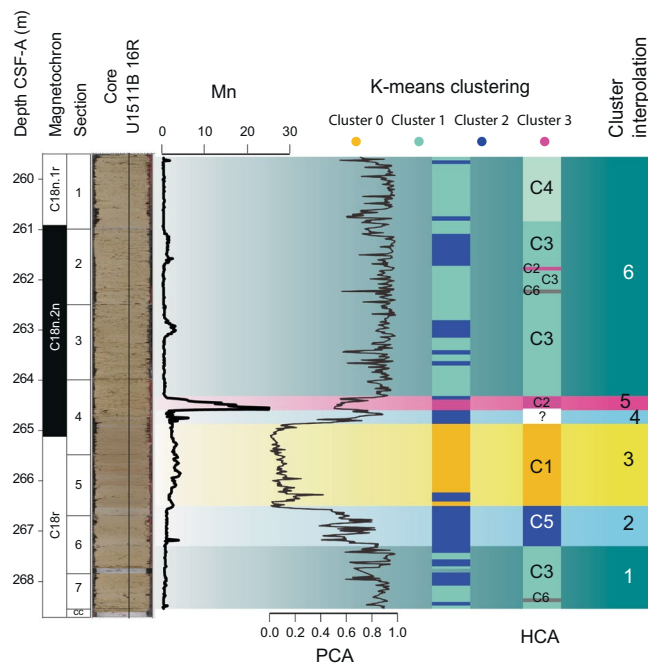


Figure 3. Summary figure for statistical analyses and interpolated cluster subdivision.

FT-IR spectra confirm the main results obtained with XRPD, revealing the presence of clay minerals (kaolinite and smectite) and quartz, as well as the absence of carbonate. Samples from within the MECO interval yield red grains, indicating the presence of poor-crystalline Fe oxides, especially hematite, not detectable by X-ray diffraction (see supplements).

To characterize the micrometric black and red grains, selected samples were investigated by Raman spectroscopy. Spectra collected on the red grains show the presence of hematite, whereas those from black grains reveal Mn oxides that can be assigned to ranciéite, todorokite, or cryptomelane. Titanium dioxides are also recognized, especially brookite and anatase, as well as traces of gypsum (see supplements).

Statistical results. *Partitioning cluster analysis (PCA).* Two major clusters were identified in the dataset, being cluster 1 dominant in the intervals 268.5–266.8 mbsf and 264.8–259.5 mbsf, and cluster 2 limited within the interval between 266.8–264.8 mbsf. Transition intervals occur before and after the cluster 2 interval, (Fig. S10).

Hierarchical cluster analysis (HCA). Two superclusters subdivided into 6 clusters and two outsiders were identified as follows (fig. S11):

Supercluster A:

Cluster 1 (C1) contains all and exclusively the samples from within 264.91–266.41-mbsf, characterized by a relative increase in smectite respect to the other minerals (fig. S5).

Cluster 2 (C2) is composed by the first sample above the C1 interval (264.66 mbsf) and a sample at 261.9 mbsf. Outsider at 264.16 mbsf.

Supercluster B:

Cluster 3 (C3) is the largest group of values and includes samples from below and above the C1 interval.

Cluster 4 (C4) composed only by samples from within 259.66–260.69 mbsf

Cluster 5 (C5) contains the three samples right below the C1 interval (266.65–167.15 mbsf)

Cluster 6 (C6) includes the samples at 262.4 and 268.44 mbsf.

Outsider at 261.26 m.

K-mean cluster analysis. This analysis was conducted on four clusters, determined by integrating the results of previous cluster analyses (Table ST1 and Fig. 3). These clusters identified four main intervals: cluster0 identifies the MECO interval, cluster1 the Pre- and post-MECO intervals, cluster2 the Pre- and Post-MECO transitions, and Cluster 3 the Mn peak interval. The mean value identified for each cluster is reported in table ST1.

Pearson correlation. A strong direct correlation occurs between Al, Si, Fe, K, and Ti, and between Cl and S, whereas Cl is anti-correlated with Si and Al. Mn, Ca, and Sr have no correlation with any element. This method was applied also to each of the six stratigraphic intervals identified by the cluster analyses and showed that the correlation coefficients change significantly from within to outside the MECO interval (fig. S12).

Discussion

The MECO event is defined according to the negative oxygen isotope anomaly at the base of the paleomagnetic Chron C18n^{7,10}. Therefore, it has been characterized mainly in pelagic carbonate successions deposited at bathyal depths, yielding well-preserved carbonate for stable isotopes measurements. Recognizing this event in successions devoid of carbonate, such as those below the CCD, is challenging. In the IODP Core U1511B the MECO is clearly recognizable thanks to the magneto-bio stratigraphy and the MS anomaly, and this represents a unique opportunity to study this event in an abyssal setting. The combination of the results of the different cluster analyses allows us to identify six stratigraphic intervals that show how the paleoceanographic conditions changed over the TAP in response to the MECO event (Fig. 3):

1. PRE-MECO (268.54–267.21 mbsf): Consists mainly of radiolarian and diatoms, with smectite (30–40%), illite (20–30%), quartz (15–20%), and kaolinite (10–15%) (Fig. 2). All the terrigenous elements (Al, Ti, Fe, and K) are directly correlated, whereas Cl is anti-correlated with Si and Al. Mn correlates moderately with MS and Fe (fig S12). K-means shows generally low values for MS and all the elements, but Cl (see supplements). This interval represents conditions with a stable circulation and a well-mixed water column, supplying oxygen at the bottom and nutrients at the surface, stimulating the productivity of bio-siliceous organisms.
2. PRE-MECO TRANSITION (267.21–266.57 mbsf): This is a 0.66 m thick interval, corresponding to ~66 kyr, considering the sedimentation rate of ref. ²⁶. Smectite, which represents 40–50% of the non-biogenic fraction, starts increasing, whereas all the other minerals decrease (Fig. 2). Trends of chemical elements change significantly, as Sr decreases whereas all detrital elements increase, as well as MS (table ST1 and Fig. 3). This expresses a lowering biogenic silica input and consequent increase in clay fraction that gets less diluted, representing the beginning of a change in the paleoceanographic conditions over the TAP towards the MECO scenario.
3. MECO (266.57–264.85 mbsf): Consists of 1.72 m of clay with biosilica, which is significantly less abundant than in the former intervals, and consists of sponge spicules and few radiolarians²⁶. This indicates a decrease in the biosiliceous plankton productivity at the surface (diatoms and radiolarians), leaving only the contribution of the sponge spicules, delivered from shallower benthic environments. This change in sediment composition is confirmed by the increasing trend of all detrital elements and MS (Fig. 1 and S3), indicating less dilution of the terrigenous fraction. Moreover, physical properties show higher sediment density, reflecting the drop of porous biosiliceous fragments and the consequent increase of clays, which are more compactable²⁶. This change induces a decrease in sedimentation rate, explaining why, by applying the value of 10 m/Myr estimated by ref. ²⁶, the duration of the MECO at this site results 172 kyr, instead of ~500 kyr observed in most of the records^{10,27}. Such shorter duration is an artefact related to a relatively poorly constrained sedimentation rate in this interval, which is based only on magnetostratigraphy and radiolarian biostratigraphy, due to the absence of carbonate microfossils²⁶. An important change occurs also in the clay's composition, with smectite increasing up to 70% and illite decreasing down to 20% (Fig. 2). As SEM analyses showed that clays in the studied core are mainly detrital (see fig. S3), the major increase in smectite within the MECO interval can express a different deep-water mass, with a larger smectite load, flowing over the TAP during the MECO. This evidence indicates a strong modification in the paleoceanographic conditions, changing the deep-water source area and inducing a more stratified water column, with consequent decrease in biosiliceous productivity at the surface. Such new conditions resulted in the deposition of more clay, especially smectite, respect to biogenic silica during the MECO. As clay particles are much more compactable, this change in sediments composition produced a decrease in the sedimentation rate, which, as stated before, is the reason for the anomalously short duration of the MECO at this site.
4. POST-MECO TRANSITION (264.85–264.57 mbsf): After the MECO there is a brief transition of ~28 kyr. In this interval all the elements shift back to Pre-MECO values, except for Mn, which presents a highly fluctuating trend (Fig. 1). K-means and Pearson correlation results also agree with this evidence (fig. S12 and ST1). These conditions are limited to a particularly thin interval above the MECO, indicating that the end of the typical MECO conditions on the TAP was rather abrupt. By comparing it with the Pre-MECO transition, it took twice longer to force the system into the MECO scenario than to switch it back.
5. MANGANESE PEAK (264.57–264.33 mbsf): A prominent Mn peak occurs in a 24 kyr long interval, 28 kyr after the end of the MECO. K-means Mn values here are 6 times higher than in the MECO and 29 times higher than in the Pre-MECO intervals (ST1). Alongside Mn, only Sr changes and shows a negative peak (fig. S2). It is worth noting the lack of correlation between Mn and Fe, which, instead, are tightly correlated in the other intervals (fig. S12). Therefore, the Mn peak is not due to an increase in hydrothermal activity, because this would have produced a concomitant increase in Fe and Sr. MS also increases in this interval and is strictly correlated with Mn (fig. S2 and S12). As the MS signal is mainly biogenic in this record (L. Chang, personal communication) such correlation may reflect a Mn rich environment that forces this element into the biogenic magnetic crystals. Recent studies demonstrate that magnetotactic bacteria can incorporate small but significant amounts of Mn, if they grow in an environment where this element is abundant^{28–31}.
6. POST-MECO (164.33–262.90): This interval is represented by the same cluster assemblage as the Pre-MECO (Fig. 3), and all Pearson values are also very similar (fig. S12). This indicates the complete restoration of Pre-MECO environmental conditions after the MECO perturbation.

Ref. ²⁶ observed that Mn is abundant throughout the entire IODP Core U1511B, as testified by several rhodochrosite nodules and high Mn content in pore waters. Mn can be delivered to this site by hydrothermal fluids, which reach the TAP since its formation, in the Late Cretaceous^{32–34}. However, no nodule or any other macroscopic Mn-bearing diagenetic feature occurs throughout the core U1511B-16R.

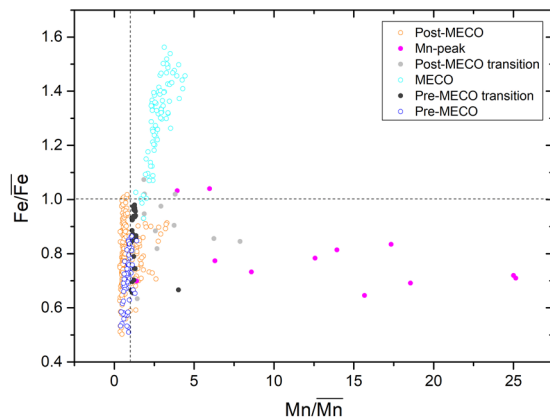


Figure 4. $\overline{Fe/Fe}$ versus $\overline{Mn/Mn}$ in the IODP Core U1511B_16R.

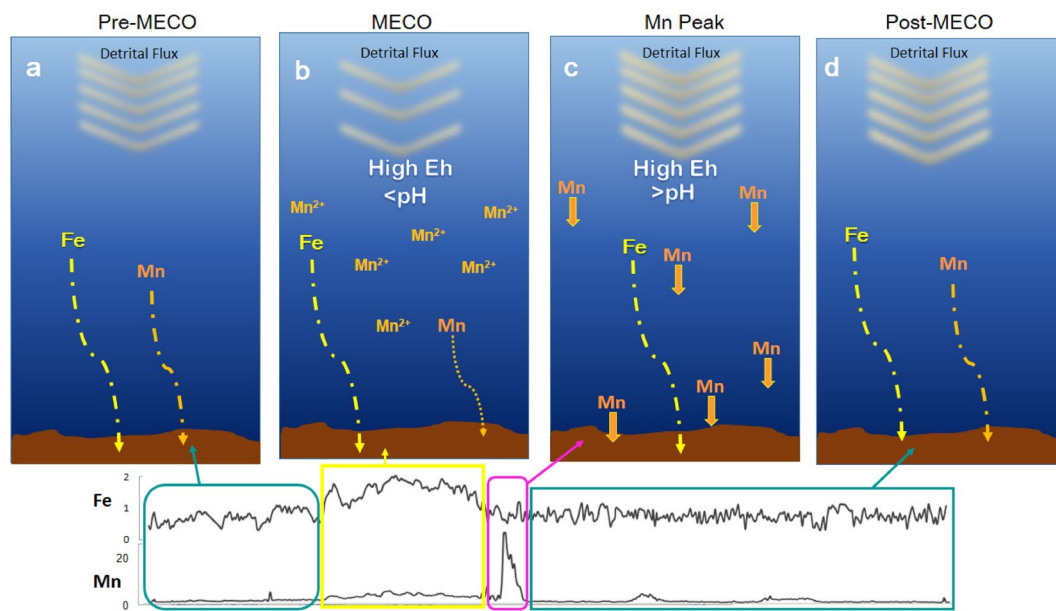


Figure 5. Environmental Model showing the oceanic bottom conditions at the Tasman Plain during the middle Eocene, respect to the variation in Mn and Fe content between the water and the sediment.

Raman spectroscopy and SEM results show that the MECO interval is characterized by abundant Fe oxides (i.e. hematite) and less Mn oxides (see supplements). The latter consists of ranciéite and possibly also of todorokite and cryptomelane. In all these compounds, Mn occurs with a high average oxidation state, about +4, +3.7, and +3.9, respectively³⁵. Moreover, Fe occurs as Fe^{3+} in hematite, which indicates high Eh water conditions. The end of the MECO event is marked by a strong Mn anomaly, without a concomitant Fe increase or any other chemical and mineralogical variation. By considering the $\overline{Fe/Fe}$ versus $\overline{Mn/Mn}$ ratios, shown in Fig. 4, we can infer that:

- 1) Pre-MECO and Post-MECO values display very similar and constant trends, indicating the restoration of Pre-MECO conditions after the event.
- 2) $\overline{Fe/Fe}$ versus $\overline{Mn/Mn}$ values are much higher within the MECO interval, indicating different conditions respect to the Pre- and Post-MECO.
- 3) The Pre-MECO transition values are similar to the Pre- and Post-MECO, whereas those of the Post-MECO transition are more scattered. Moreover, while $\overline{Fe/Fe}$ values in the latter interval are close to those in the Pre- and Post-MECO, the $\overline{Mn/Mn}$ ratio rises up to ~8 times higher than the mean of the entire core. This indicates that Mn is extremely more sensitive than Fe to the changes occurred at the end of the MECO.
- 4) In the Mn-peak interval, $\overline{Fe/Fe}$ still shows values close to those of the Pre and Post-MECO, whereas $\overline{Mn/Mn}$ values soar up to ~25 times higher than the mean of the entire core. Considering that Mn is the only element showing an anomaly in this interval and that Mn oxides are stable only under either basic pH (>8) or high Eh conditions³⁶, major redox changes must have occurred over the TAP during and after the MECO. The presence of hematite and Mn with high average oxidation state, both within and out of the

MECO interval, indicates that high Eh conditions existed over the TAP throughout all the studied period. Thus, Eh was not a main controlling factor for Mn in this case. Consequently, a strong increase in pH must have occurred from the MECO to the Post-MECO, which produced the sudden precipitation of the dissolved Mn and the anomalous accumulation of Mn oxides within the sediments. The tight correlation between Mn and MS within the MECO and the Mn peak intervals suggests that Mn oxides precipitation could have also been catalysed by microbial activity, which increased during the MECO.

These considerations provide useful insights to constrain the paleoceanographic conditions over the TAP before, during, and after the MECO event (Fig. 5). Before the MECO the Tasman Sea was characterized by a well-mixed water column, with a persistent nutrients supply to the surface that sustained biosiliceous productivity. The bottom of the TAP was relatively well ventilated, with deep water delivering detrital smectite and illite. During the MECO the oceanographic conditions changed dramatically, as the water column became more stratified and the biosiliceous productivity was almost suppressed. Additionally, a switch in the bottom water masses delivered more smectite and lowered the pH . The only way to decrease the pH at abyssal depth is by introducing a more acid water mass³⁷. In such more acid but still oxidizing conditions, Fe oxides still precipitated, whereas Mn remained dissolved and increased its concentration in the bottom water. Yet, some Mn oxides still could precipitate and became slightly concentrated within the MECO interval due to the lower sedimentation rate, which explains the slight increase in Mn respect to the Pre-MECO. Alternatively, such slight increase can be due more detrital Mn delivered during the MECO. After the MECO, deep circulation switched back to the Pre-MECO conditions, with water masses delivering less smectite and characterized by relatively high Eh and high pH . This produced a strong and abrupt increase in pH , which induced the sudden precipitation of the Mn that remained concentrated in the water during the MECO. Afterwards, the system got re-equilibrated to the same conditions as before the MECO.

The changes described represent the response of the complex oceanographic circulation of the SO to the MECO climatic warming^{4,38}. Major circulation changes have been described in previous studies associated with the MECO climatic warming, at surface to bathyal depths^{4,10,11,26,39,40}. Here we show that modifications occurred also in the abyssal circulation of the SO, with the inflow of more acid bottom water.

Evidence of ocean acidification during the MECO was presented by ref. ¹⁰. Low pH bottom waters are necessary to explain the observations at Site U1511, and this indicates that acidification reached abyssal depths, at least in the SO. In order to acidify the bottom waters over the TAP, a large amount of inorganic carbon must have entered into the SO, and kept stored in the deep environment, which requires a stratified water column, as observed at the studied site, and an efficient biologic pump⁴¹. Such configuration could have maintained low pH and warming conditions for hundreds of thousand years, so explaining in part the conundrum related to this event^[14.] On the other hand, the source of carbon that triggered the acidification still remains uncertain and perhaps it is related to C-cycle instability induced by orbital forcing²⁷. Even though the main trigger of the MECO is still unclear, we showed that oceanic circulation played a key role for the development of this event.

Methods

A total of 37 samples were collected from the Core U1511B-16R. Part of the material was grounded and used for XRPD, XRF, and FT-IR analyses, whereas the rest, untreated, was used for SEM-EDS and Raman spectroscopy analyses.

Scanning electron microscopy and energy dispersive spectroscopy (SEM-EDS). The samples were coated in carbon and then analysed at the Scanning Electron Microscopy Laboratory of the Geosciences Institute of the University of São Paulo (LabMev - IGc - USP). The scanning electron microscope (SEM) used is a LEO 440, by LEO Electron Microscopy Ltd. Equipped with an X-ray Dispersive Energy Spectrometer (EDS) with a Si (Li) solid-state detector controlled by Inca 300 software from Oxford Ltd. The analyses were conducted at 20 kV of Acceleration Voltage, with working distance from 5 to 18 mm, and an EDS Live Quotation Time of 100 s.

X-ray powder diffraction (XRPD). Two types of XRPD analyses were performed:

Conventional XRPD analysis were performed on 7 samples at the X-Ray diffraction Laboratory of the Geoscience Institute of the University of Brasilia using a Rigaku Ultima IV with a copper anode ($\lambda = 1.5406 \text{ \AA}$), working at 35 kV and 15 mA. The samples chosen were the closest to the most representative of each cluster identified with the HCA. Two samples were chosen from the pre-MECO, pre-MECO transition, and post-MECO intervals, respectively, and one sample from the MECO interval.

As the sediments contain 90–99% of clay, measurements were taken in four steps (fig. S4), according to the standard procedure for clay treatment⁴²:

- Bulk XRD analyses: the sample was gently pulverized in a jade mortar and inserted in the sample holder, XRD measurements were taken on the whole sample;
- Clay fraction (CF) XRD analyses: the clay fraction was separated from the bulk sediment and analysed separately to better visualize the clay content. The bulk sample was washed in an ultrasonic bath with deionized water to remove the halite that causes flocculation. After re-dispersion in water, the mixture was centrifuged at 750 rpm for 7 min. The silt fraction deposited, while the clay fraction remained in suspension. This suspension, transferred to another tube, was centrifuged at 3,000 rpm for 30 min. The clay fraction decanted by centrifugation at 3000 rpm, was spread on a glass slide, using a spatula, with repeated movements in the same direction to orient the clays. The purpose of the orientation is to highlight the plan [001] of the clay minerals. The small dimensions of clay minerals and their low crystalline organization do not favour the formation

of intense reflections, which become even less important when the clay fraction contains highly crystalline minerals, such as quartz, calcite, or even some oxides. The orientation of the samples places the basal surfaces - plane [001] - of the various particles parallel to each other, simulating a larger crystal. The sample oriented on the slide is left to air for drying, before measurement by XRD.

- CF XRD analyses after vacuum solvation in ethylene glycol: The process consists of leaving the slide used for the previous measurement in an atmosphere of ethylene glycol for about 12 hours, favouring the penetration of the compound in the interlayer spaces of the expanding clay minerals. The slide is then analysed by XRD, allowing the verification of the possible increase in interplanar distances.
- CF XRD analyses after heating: during this process, the previously measured slide is heated to a temperature of 490 °C, for 4.5 hours. After cooling, the sample is analysed and changes in the position of the peaks, due to the loss of material from the interlayer site or the collapse of the structure of some minerals, can be verified.

Mineral identification was done using the Jade 9 software with the ICDD PDF-2 (2010) and ICDD PDF-4 (2010) databases.

Bench-top XRPD analyses were performed with an Olympus BTX II with a Co anode ($\lambda = 1.789 \text{ \AA}$) in the Centro Oceanográfico de Registros Estratigráficos (CORE) laboratory of the Oceanographic Institute of the University of São Paulo. Bulk mineralogy was analysed in all the 37 samples for statistical purposes. An aliquot of about 1 cm^3 of sediment was gently pulverized in a jade mortar by hand and sieved through a $63 \mu\text{m}$ sieve. Then, about 15 mg of powder were analysed at 30 kV and 0.326 mA, over a range $5\text{--}55^\circ 2\theta$, with a step size of 0.05° , and 100 exposures over 22 minutes. Mineral identification was done using the PANalytical High Score Plus software equipped with the Crystal Structure Database⁴³, the Crystallography Open Database, and the collection from the International Centre for Diffraction Data (Newtown Square, PA).

Fourier-transform infrared spectroscopy (FT-IR). FT-IR spectra were collected at the Infrared Spectroscopy Laboratory, Department of Science, Roma Tre University, using a Nicolet iS50 FT-IR spectrometer equipped with a DTGS detector and a KBr beamsplitter. The nominal resolution was 4 cm^{-1} , and 64 scans were averaged for each sample and for the background. Samples were prepared as pellets containing about 1 mg of powdered sample in 200 mg of KBr.

Raman spectroscopy. For each sample, we performed several point analyses by Raman spectroscopy, in order to check for possible inhomogeneities. Because of the high sensitivity of Mn and Fe oxides to the laser heating^{44,45}, Raman measurements were performed with a progressively increasing laser power, in order to avoid degradation of the samples. Raman measurements were performed at the Raman Spectroscopy Laboratory, Department of Science, Roma Tre University, at room temperature using an inVia Renishaw Raman equipped with a diode laser (532 nm, output power 50 mW), an edge filter to select the Raman scattering avoiding the elastic contribution, a 1800 lines/mm diffraction grating and a Peltier cooled 1024×256 pixel CCD detector. Samples were mounted on the manual stage of a Leica DM2700 M confocal microscope. Laser beam focusing and collection of Raman signals were realized with a 100x objective (with 2 mW and 5 accumulations of 10 s each, in the range of $200\text{--}900 \text{ cm}^{-1}$). The Raman spectrometer was calibrated prior to the measurements using a Si wafer and by performing the automatic offset correction. The spectra acquisition and data analyses were performed using WiRE and Origin softwares. The peak positions are estimated to be accurate to at least $\pm 2 \text{ cm}^{-1}$.

X-Ray Fluorescence (XRF) scanning. XRF scanner data of the Core U1511B-16R were obtained with an AVAATECH scanner XRF at the IODP base in College Station (Texas, USA) and are available in the IODP online data repository⁴⁶. Data have been normalized to minimize analytical errors by dividing each entry by the mean value of all the counts of the respective element⁴⁷.

Statistical analyses. *Hierarchical cluster analysis (HCA).* XRPD data collected with the Olympus BTX II Bench-top XRD were analysed with the PANalytical High Score Plus software for cluster analysis.

Partitioning cluster analysis (PCA). this method was applied to the XRF, magnetic susceptibility, and reflectance data of the Core U1511B-16R. The fuzzy *c*-means (FCM) algorithm proposed by ref. ⁴⁸ was used for the partitioning approach. This algorithm refers to a soft method of clustering, in which each sample of a dataset can belong to more than one cluster simultaneously. The clustering values are expressed in terms of a variable called pertinence, which fluctuates within a continuous interval $[0, 1]$ ⁴⁹. A sample with pertinence values close to zero indicates a poor similarity with the cluster, whereas pertinence close to one represents high similarity.

K-means cluster analysis. K-means clustering was applied to XRF and MS data. This is a method divides the number of observations in a defined number (K) of clusters. Each cluster is characterized by the mean value of the data contained. Each observation belongs to the cluster with the closest mean, which represents the prototype of the respective cluster.

Pearson correlation. the Pearson correlation coefficient was applied to the XRF and MS data to identify correlations among them. The Pearson correlation coefficient measures the linear correlation between two variables and is expressed with a value between +1 and -1. A value equal to 1 represents a direct correlation between the two variables, describable by a linear equation in which Y and X increase together. A value equal to -1 represents an inverse correlation, describable with a linear equation in which Y decreases as X increases. When the Pearson coefficient equals to 0 there is no linear correlation between the two variables. The Pearson correlation

was applied to the series of the entire Core U1511B-16R, and also on individual stratigraphic intervals, identified by interpolating k-means clustering, PCA, and HCA.

Data availability

SEM-EDS, XRD, FT-IR, Raman spectroscopy and statistical data presented in this work can be obtained from the corresponding author upon request. Magnetic susceptibility and XRF scanning data can be downloaded from <http://iodp.tamu.edu/LORE/>.

Received: 18 December 2019; Accepted: 1 April 2020;

Published online: 21 April 2020

References

- Zachos, J. C., Gerald, R. D. & Richard, E. Z. An early Cenozoic perspective on greenhouse warming and carbon-cycle dynamics. *Nature* **451**, 717–720 (2008).
- Inglis, G. N. *et al.* Descent toward the Icehouse: Eocene sea surface cooling inferred from GDGT distributions. *Paleoceanography and Paleoclimatology* **30**, 7, 1000–1020 (2015).
- Anagnostou, E. *et al.* Changing atmospheric CO₂ concentration was the primary driver of early Cenozoic climate. *Nature* **533**, 7603, 380 (2016).
- Cramwinckel, M. J. *et al.* Surface-circulation change in the Southern Ocean across the Middle Eocene Climatic Optimum: inferences from dinoflagellate cysts and biomarker paleothermometry.
- Cramwinckel, M. J. *et al.* Synchronous tropical and polar temperature evolution in the Eocene. *Nature* **559**, 7714, 382 (2018).
- Jovane, L. *et al.* The middle Eocene climatic optimum event in the Contessa Highway section, Umbrian Apennines, Italy. *Geological Society of America Bulletin* **119**, 3–4, 413–427 (2007).
- Jovane, L. *et al.* Astronomical calibration of the middle Eocene Contessa Highway section (Gubbio, Italy). *Earth and Planetary Science Letters* **298**, 1–2, 77–88 (2010).
- Bohaty, S. M. & James, C. Zachos. Significant Southern Ocean warming event in the late middle Eocene. *Geology* **31**, 11, 1017–1020 (2003).
- Edgar, K. M. *et al.* New biostratigraphic, magnetostratigraphic and isotopic insights into the Middle Eocene Climatic Optimum in low latitudes. *Palaeogeography, Palaeoclimatology, Palaeoecology* **297**, 3–4, 670–682 (2010).
- Bohaty, S. M., *et al.* Coupled greenhouse warming and deep-sea acidification in the middle Eocene. *Paleoceanography* **24**, 2 (2009).
- Bijl, P. K. *et al.* Transient Middle Eocene atmospheric CO₂ and temperature variations. *Science* **330**, 6005, 819–821 (2010).
- Marvel, K. & Céline, B. Identifying external influences on global precipitation. *Proceedings of the National Academy of Sciences* **110**, 48, 19301–19306 (2013).
- Rego, E. S. *et al.* Mineralogical evidence for warm and dry climatic conditions in the Neo-Tethys (eastern Turkey) during the middle Eocene. *Palaeogeography, Palaeoclimatology, Palaeoecology* **501**, 45–57 (2018).
- Sluijs, A. *et al.* A middle Eocene carbon cycle conundrum. *Nature Geoscience* **6**, 6, 429 (2013).
- Röhl, U. *et al.* Sea level and astronomically induced environmental changes in Middle and Late Eocene sediments from the East Tasman Plateau. *Washington DC American Geophysical Union Geophysical Monograph Series* **151**, 127–151 (2004).
- Berner, R. A. A new geochemical classification of sedimentary environments. *Journal of Sedimentary Research* **51**, 2, 359–365 (1981).
- Post, J. E. Manganese oxide minerals: Crystal structures and economic and environmental significance. *Proceedings of the National Academy of Sciences* **96**, 7, 3447–3454 (1999).
- Hem, J. D. Chemical equilibria affecting the behavior of manganese in natural water. *Hydrological Sciences Journal* **8**, 3, 30–37 (1963).
- Hem, J. D. Chemical factors that influence the availability of iron and manganese in aqueous systems. *Geological Society of America Bulletin* **83**, 2, 443–450 (1972).
- Brookins, D. G. “Eh-pH Diagrams for Geochemistry.” Springer, Berlin, Heidelberg. 68-70. B45, (1988)
- Langmuir, D. “Aqueous environmental.” Geochemistry Prentice Hall: Upper Saddle River, NJ (1997).
- Tebo, B. M. *et al.* Biogenic manganese oxides: properties and mechanisms of formation. *Annu. Rev. Earth Planet. Sci.* **32**, 287–328 (2004).
- Savian, J. F. *et al.* Enhanced primary productivity and magnetotactic bacterial production in response to middle Eocene warming in the Neo-Tethys Ocean. *Palaeogeography, Palaeoclimatology, Palaeoecology* **414**, 32–45 (2014).
- Savian, J. F. *et al.* Environmental magnetic implications of magnetofossil occurrence during the Middle Eocene Climatic Optimum (MECO) in pelagic sediments from the equatorial Indian Ocean. *Palaeogeography, palaeoclimatology, palaeoecology* **441**, 212–222 (2016).
- Rodelli, D. *et al.* High-resolution integrated magnetobiostratigraphy of a new middle Eocene section from the Neotethys (Elazığ Basin, eastern Turkey). *GSA Bulletin* **130**, 1–2, 193–207 (2018).
- Sutherland, R., Dickens, G. R., Blum, P. and the Expedition 371 Scientists, Tasman Frontier Subduction Initiation and Paleogene Climate. Proceedings of the International Ocean Discovery Program, 371: College Station, TX (International Ocean Discovery Program). <https://doi.org/10.14379/iodp.proc.371.108.2019>.
- Giorgioni, M. *et al.* Carbon cycle instability and orbital forcing during the Middle Eocene Climatic Optimum. *Scientific Reports* **9**, 1, 9357 (2019).
- Keim, C. N., Lins, U. & Farina, M. Manganese in biogenic magnetite crystals from magnetotactic bacteria. *FEMS microbiology letters* **292**, 2, 250–253 (2009).
- Tanaka, M. *et al.* Highest levels of Cu, Mn and Co doped into nanomagnetic magnetosomes through optimized biomineralisation. *Journal of Materials Chemistry* **22**, 24, 11919–11921 (2012).
- Prozorov, T. *et al.* Manganese incorporation into the magnetosome magnetite: magnetic signature of doping. *European Journal of Mineralogy* **26**, 4, 457–471 (2014).
- Bin, H. M. *et al.* “Presence of Biogenic Magnetite in Ferromanganese Nodules”. Environmental microbiology reports (2020).
- Gaina, C. *et al.* The tectonic history of the Tasman Sea: a puzzle with 13 pieces. *Journal of Geophysical Research: Solid Earth* **103**, B6, 12413–12433 (1998).
- Sutherland, R. Basement geology and tectonic development of the greater New Zealand region: an interpretation from regional magnetic data. *Tectonophysics* **308**, 3, 341–362 (1999).
- Sutherland, R. *et al.* Continental-scale geographic change across Zealandia during Paleogene subduction initiation. *Geological*. <https://doi.org/10.1130/G47008.1> (2020).
- Chalmin, E. F. F. & Gordon, E. Brown A pre-edge analysis of Mn K-edge XANES spectra to help determine the speciation of manganese in minerals and glasses. *Contributions to Mineralogy and Petrology* **157**, 1, 111–126 (2009).
- Roy, S. Genetic diversity of manganese deposition in the terrestrial geological record. *Geological Society, London, Special Publications* **119**, 1, 5–27 (1997).
- Sarmiento, J. L. & Bender, M. Carbon biogeochemistry and climate change. *Photosynthesis Research* **39**, 3, 209–234 (1994).

38. Nelson, C. S. & Penelope, J. C. History of oceanic front development in the New Zealand sector of the Southern Ocean during the Cenozoic—a synthesis. *New Zealand Journal of geology and geophysics* **44.4**, 535–553 (2001).
39. Warnaar, J. *et al.* Orbitally forced climate changes in the Tasman sector during the Middle Eocene. *Palaeogeography, Palaeoclimatology, Palaeoecology* **280.3–4**, 361–370 (2009).
40. Moebius, I. O. Friedrich & Howie, D. Scher Changes in Southern Ocean bottom water environments associated with the Middle Eocene Climatic Optimum (MECO). *Palaeogeography, palaeoclimatology, palaeoecology* **405**, 16–27 (2014).
41. Marinov, I. *et al.* “Impact of oceanic circulation on biological carbon storage in the ocean and atmospheric pCO₂”. *Global Biogeochemical Cycles* **22.3** (2008).
42. Moore, D M & Robert C. R. Jr. X-ray Diffraction and the Identification and Analysis of Clay Minerals. Oxford University Press (OUP) (1989).
43. Downs, R. T. & Michelle, H.-W. The American Mineralogist crystal structure database. *American Mineralogist* **88.1**, 247–250 (2003).
44. Bernardini, S. *et al.* Raman spectroscopy and laser-induced degradation of groutellite and ramsdellite, two cathode materials of technological interest. *RSC advances* **10**, 923 (2020).
45. de Faria, D. L. A. & Francisco, N. L. Heated goethite and natural hematite: can Raman spectroscopy be used to differentiate them? *Vibrational Spectroscopy* **45.2**, 117–121 (2007).
46. <http://iodp.tamu.edu/LORE>
47. Weltje, G. J. & Tjallingii, R. Calibration of XRF core scanners for quantitative geochemical logging of sediment cores: theory and application. *Earth and Planetary Science Letters* **274.3–4**, 423–438 (2008).
48. Bezdek, J. C., Ehrlich, R. & Full, W. FCM: The fuzzy c-means clustering algorithm. *Computers & Geosciences* **10(2-3)**, 191–203 (1984).
49. Dekkers, M. J., Langereis, C. G., Vriend, S. P., Van Santvoort, P. J. M. & De Lange, G. J. Fuzzy c-means cluster analysis of early diagenetic effects on natural remanent magnetisation acquisition in a 1.1 Myr piston core from the Central Mediterranean. *Physics of the Earth and Planetary Interiors* **85(1-2)**, 155–171 (1994).

Acknowledgements

The authors thank the personnel of the XRD laboratory at the Geoscience Institute of the University of Brasilia, of the Scanning Electron Microscopy Laboratory of the Geosciences Institute of the University of São Paulo, of the Raman equipment of the Brazilian Research Unity in Astrobiology – NAP Astrobio Raman of the University of São Paulo, of the Infrared Spectroscopy Laboratory and Raman Spectroscopy Laboratory of the Department of Science of the Roma Tre University for the technical assistance during the analyses. This study was financed in part by the Coordenação de Aperfeiçoamento de Pessoal de Nível Superior - Brasil (CAPES) - Finance Code 001 that granted the PhD fellowship of F.C. and the participation of M.G. in the IODP Expedition 371. This research is sponsored by the Fundação de Amparo à Pesquisa do Estado de São Paulo (FAPESP projects 11/22018–3; 16/24946–9; 18/17061–6).

Author contributions

F.C. corresponding author; XRD, Raman spectroscopy, SEM-EDS, and HCA analyses; integration and interpretation of the data; writing of the manuscript. S.B., FT-IR and Raman spectroscopy analyses and interpretation, revision of the manuscript. M.G., description and selection of the samples, interpretation of the XRF data, revision of the manuscript. G.L.X.S., PCA analysis and interpretation, revision of the manuscript. A.I.M.N., Pearson correlation and K-means analyses and interpretation, revision of the manuscript. L.J., PhD supervisor of F.C., revision of the manuscript.

Competing interests

The authors declare no competing interests.

Additional information

Supplementary information is available for this paper at <https://doi.org/10.1038/s41598-020-63525-3>.

Correspondence and requests for materials should be addressed to F.C.

Reprints and permissions information is available at www.nature.com/reprints.

Publisher’s note Springer Nature remains neutral with regard to jurisdictional claims in published maps and institutional affiliations.



Open Access This article is licensed under a Creative Commons Attribution 4.0 International License, which permits use, sharing, adaptation, distribution and reproduction in any medium or format, as long as you give appropriate credit to the original author(s) and the source, provide a link to the Creative Commons license, and indicate if changes were made. The images or other third party material in this article are included in the article’s Creative Commons license, unless indicated otherwise in a credit line to the material. If material is not included in the article’s Creative Commons license and your intended use is not permitted by statutory regulation or exceeds the permitted use, you will need to obtain permission directly from the copyright holder. To view a copy of this license, visit <http://creativecommons.org/licenses/by/4.0/>.

© The Author(s) 2020